# Achieving stable anionic redox chemistry in Li-excess O2-type layered oxide cathode via chemical ion-exchange strategy

Xin Cao, Haifeng Li, Yu Qiao,\* Min Jia, Ping He, Jordi Cabana and Haoshen Zhou\*

X. Cao, Dr. Y. Qiao, M. Jia, Prof. H. Zhou

Energy Technology Research Institute, National Institute of Advanced Industrial Science and Technology (AIST), 1-1-1, Umezono, Tsukuba 305-8568, Japan.

E-mail: kyou.qiaoyu09206@aist.go.jp (Y. Q.)

E-mail: <u>hs.zhou@aist.go.jp (H. Z.)</u>

H. Li, Prof. J. Cabana,

Department of Chemistry, University of Illinois at Chicago, Chicago, Illinois 60607, United States

Prof. P. He, Prof. H. Zhou

Center of Energy Storage Materials & Technology, College of Engineering and Applied Sciences, Jiangsu Key Laboratory of Artificial Functional Materials, National Laboratory of Solid State Microstructures, and Collaborative Innovation Center of Advanced Microstructures, Nanjing University, Nanjing 210093, P. R. China E-mail: <a href="mailto:hszhou@nju.edu.cn">hszhou@nju.edu.cn</a> (H. Z.)

X. Cao, M. Jia, Prof. H. Zhou

Graduate School of System and Information Engineering, University of Tsukuba, 1-1-1, Tennoudai, Tsukuba 305-8573, Japan

Keywords: lithium-ion batteries, layered cathode material, anionic redox reactions, ion exchange, structural stability

#### **Abstract**

Triggering oxygen-centered redox activity has been regarded as a promising way to boost the capacity of layered cathode materials for Li/Na-ion batteries. However, irreversible loss of lattice oxygen aggravates a structural distortion to a spinel phase, which leads to severe voltage decay and capacity degradation. Herein, via a specific chemical ion-exchange procedure, the sodium within the alkali metal layer of a P2-type oxide precursor has been substituted by Li while the transition metal layer can be preserved, resulting in the formation of a Li-excess O2-type layered oxide cathode, Li<sub>0.66</sub>[Li<sub>0.12</sub>Ni<sub>0.15</sub>Mn<sub>0.73</sub>]O<sub>2</sub> (LLNMO). Through systematic in/ex-situ and surface/bulk characterization (hard X-ray absorption spectroscopy, operando Raman/XRD and differential electrochemical mass spectroscopy, etc.), the redox reversibility and structural stability of LLNMO have been comprehensively demonstrated. More intriguingly, being evolved from the same sodium-based precursor, a similar O2-type compound generated by an equivalent electrochemical exchange procedure presents severely irreversible behavior on both structural and redox processes. On the aspect of materialogy and methodology, the sharp comparison results have elucidated that the chemical ion-exchange strategy can be regarded as an efficient way to design new classes of high-capacity cathode candidates which possess stable anionic redox activity and enhanced structural stability simultaneously.

#### 1. Introduction

Oxygen-centered redox chemistry has been regarded as a promising way to achieve high energy density in current battery systems.<sup>[1]</sup> Oxygen redox reactions can be triggered in layered cathodes when transition metal (TM) ions in TM layers are partially substituted by either vacancies or other light elements that are not redox active (Li, Na and Mg).[2] With that, several cathodes have broken the capacity bottleneck originating solely from conventional TM-centered redox activities.<sup>[3]</sup> For instance, typical Li-rich layered oxides, xLi<sub>2</sub>MnO<sub>3</sub>·(1-x)LiTMO<sub>2</sub> (TM= Mn, Ni and Co), where transition metals (TM) are partly replaced by Li, deliver a high discharge capacity exceeding 250 mAhg<sup>-1</sup>.<sup>[4]</sup> Besides, oxygen redox usually occurs at higher voltage (above ~4.0 V vs Li/Li<sup>+</sup>) compared with other anionic redox processes (e.g. sulfur, below ~2.8 V vs Li/Li<sup>+</sup>).<sup>[5]</sup> However, the utilization of attractive anionic redox chemistry is generally accompanied by irreversible lattice oxygen loss, which is induced by deep oxygen oxidation reactions in high voltage region.<sup>[6]</sup> More serious, lattice oxygen release inevitably triggers a deleterious layered-to-spinel phase transformation because transition metal ions irreversibly migrate from the TM layer to the alkali layer, resulting in durative output-voltage decay, capacity degradation and irreversibility.<sup>[7]</sup> Notably, despite delivering more than 300 mAh g<sup>-1</sup> charge capacity, Li<sub>2</sub>MnO<sub>3</sub> (Li[Li<sub>0.33</sub>Mn<sub>0.67</sub>]O<sub>2</sub>), which operates solely through oxygen-centered oxidation reactions, displays limited reversible discharge capacities with severe voltage fading during long-term cycling, which can be attributed to irreversible oxidation of lattice oxygen to O<sub>2</sub> gas and the nucleation and growth of spinel domains upon cycling.<sup>[8]</sup>

Synthetic methods based on ion exchange constitute a universal tool for exploring metastable inorganic materials, which have crystal frameworks analogous to the parent phases but with novel chemical composition. [9] In the field of rechargeable batteries, this route of synthesis has been used frequently in designing novel electrode materials for lithium storage, using both chemical routes in various media (i.e., hexanol, water and molten salt) and electrochemical approaches.<sup>[10]</sup> More specifically, through Li<sup>+</sup>/Na<sup>+</sup> ion exchange reactions, Li compounds can inherit some structure features of their parent Na layered oxides, which cannot be directly achieved via direct synthesis methods.<sup>[11]</sup> For instance, Paulsen et al. developed O2-type layered Li<sub>2/3</sub>Ni<sub>1/3</sub>Mn<sub>2/3</sub>O<sub>2</sub> by ion exchange, a phase which displays higher reversible capacity and excellent structure stability than an O3-type analogue (LiNi<sub>1/2</sub>Mn<sub>1/2</sub>O<sub>2</sub>) since the O2-type stacking (ABCBA) can be preserved upon cycling, whereas O3-type layered structure (R3m) converts to a spinel phase (Fd3m).[12] The robust structure stability might benefit from the fact that the O2-type structure restricts the movements of transition metals within the Li layer, which promotes the reversibility of the cation migration and thereby suppresses the formation of spinel phase upon cycling.<sup>[13]</sup> Based on these advantages of O2 stackings, it is urgent to develop a class of promising Li-excess cathode materials via electrochemical/chemical ion-exchange method to address the drawbacks of conventional Li-rich cathodes. Furthermore, it is also imperative to clarify the existence of cationic/anionic redox reactions, lattice

oxygen evolution, and phase transition within such Li-excess O2-type oxides to establish the underlying mechanism and potential applications of oxygen redox chemistry.

Herein, Li-excess O2-type Li<sub>0.66</sub>[Li<sub>0.12</sub>Ni<sub>0.15</sub>Mn<sub>0.73</sub>]O<sub>2</sub> was achieved from the corresponding P2-type Na analog via chemical Li<sup>+</sup>/Na<sup>+</sup> ion exchange, where the layered structure and oxygen stacking was preserved yet Na<sup>+</sup> ions within alkali metal layers were substituted by Li<sup>+</sup> ions. Compared with an O2-type electrode generated by conducting the cation exchange electrochemically instead, irreversible oxygen behavior and a harmful layered-to-spinel phase transformation can be effectively suppressed within LLNMO, despite being generated from the same Na-based precursor. Moreover, the irreversible/reversible oxygen/TM redox behaviors of LLNMO are comprehensively unraveled and quantified through hard X-ray absorption spectroscopy (XAS), operando differential electrochemical mass spectroscopy (DEMS) and X-ray photoelectron spectroscopy (XPS). Furthermore, we establish that a reversible structure evolution without 3d metals migration can be achieved during Li<sup>+</sup> (de)intercalation processes, resulting in high reversibility of anionic/cationic redox and structural evolution of LLNMO. These findings have elucidated that chemical ion exchange avenue can be regarded as an efficient way to resolve the issues of voltage decay and capacity fade within Li-rich layered oxides.

#### 2. Results and Discussion

### 2.1 Synthesis, Structure Characterization and Electrochemistry

The Li-excess O2-type Li<sub>0.66</sub>[Li<sub>0.12</sub>Ni<sub>0.15</sub>Mn<sub>0.73</sub>]O<sub>2</sub> (defined as LLNMO) was synthesized through a chemical ion exchange method from Na-deficient precursor Na<sub>0.66</sub>[Li<sub>0.12</sub>Ni<sub>0.15</sub>Mn<sub>0.73</sub>]O<sub>2</sub> (labeled as NLNMO). Inductively Coupled Plasma (ICP) analysis and XRD were employed to evaluate the composition and crystal structure of NLNMO (Figure 1a, Tables S1 and S2). The nearly identical mol ratio of elements obtained from ICP test was in good agreement with the sample composition. Rietveld refinement of XRD was conducted by General Structure Analysis System (GSAS-II), delivering a goodness of fitting with low error values of  $\chi^2$  (1.76) and  $R_{wp}$ (4.71%). Moreover, the peaks shown in the calculated pattern fit well with the experimental XRD data, expressing an accurate indexing with a hexagonal P2-type arrangement with the space group P63/mmc. The calculated lattice parameters of NLNMO are a = b = 2.84(6) Å, c = 14.42(5) Å,  $\alpha = \beta = 90^{\circ}$ ,  $\gamma = 120^{\circ}$ . Therefore, the NLNMO is a typical P2-type layered oxide derivative of P2 layered Na2/3MnO2 in which part of Mn<sup>3+/4+</sup> ions are substituted by Li<sup>+</sup> and Ni<sup>2+</sup> ions.<sup>[14]</sup> More specifically, the Li, Ni and Mn ions within NLNMO randomly occupy the octahedral sites between the AB oxide layers and Na occupies the trigonal prismatic sites within the alkali metal layer, delivering an ABBA oxygen stacking sequence (Figure 1a inset).

After chemical ion exchange in molten salts (LiNO<sub>3</sub> and LiCl), the chemical formula of LLNMO was also confirmed as Li<sub>0.66</sub>[Li<sub>0.12</sub>Ni<sub>0.15</sub>Mn<sub>0.73</sub>]O<sub>2</sub> by ICP (Table S3), indicating only sodium ions within the alkali metal layer were substituted by lithium ions from molten salts. In addition, XRD of LLNMO and the corresponding Rietveld refinement results revealed a layered structure with a hexagonal O2-type

arrangement with space group P6<sub>3</sub>mc (Figure 1b and Table S4). The calculated lattice parameters (a = b = 2.84(6) Å, c = 14.42(5) Å,  $\alpha = \beta = 90^{\circ}$ ,  $\gamma = 120^{\circ}$ ) of LLNMO are also similar to values for O2-type Li<sub>2/3</sub>Ni<sub>1/3</sub>Mn<sub>2/3</sub>O<sub>2</sub> in the literature.<sup>[15]</sup> The phase transition from P2 structure to O2 structure is due to the rearrangement of the layers to make octahedral sites for lithium by gliding every second Li/Ni/Mn layer in two directions (i.e., A becomes B or C) since lithium strongly favors octahedral arrangements whereas sodium can adopt prismatic or octahedral coordination within layered structures.<sup>[16]</sup>

The electrochemical performance of NLNMO and LLNMO as cathode materials in Li half-cells was evaluated by galvanostatic cycling (Figures 1c and 1d). NLNMO presents a sloping voltage profile upon initial charge, similar to the first charge curve in a Na half-cell (Figure S1), indicating the Na extraction from NLNMO also occurs in Li half-cells. After this initial charge, NLNMO subsequently exhibits charge/discharge curves with a typical "S-shape". These curves are similar to LLNMO in Li half-cell, suggesting lithium ion becomes the dominating charge carrier within NLNMO after the initial Na<sup>+</sup> extraction. Nonetheless, it is possible that a limited amount sodium ions could conceivably still reinsert into the alkali metal layer during this process. After only a couple of cycles, a drastic downshift of the discharge voltage can be observed in NLNMO, whereas the voltage profile of the second discharge was almost identical to that of the first discharge for LLNMO. To further clarify the long-term voltage retention of these two cathodes, cycling for an additional 10 cycles was performed (Figures S2 and S3). The negligible voltage decay of

LLNMO is in stark contrast with the severe fade of NLNMO under the same electrochemical cycling conditions. Besides, LLNMO delivered a marginal irreversible capacity of 2.9 mAhg<sup>-1</sup> upon second discharge, in comparison with the large irreversible capacity of 30 mAh g<sup>-1</sup> for NLNMO, implying more stable and reversible electrochemical behavior in LLNMO.

The structural evolution of NLNMO and LLNMO during the initial two cycles were further investigated (Figures 2a and 2b). Compared with pristine state, the (002) peak of NLNMO shifted to higher angle and other peaks disappeared, which arises from the substitution of Li<sup>+</sup> for Na<sup>+</sup> via the electrochemical ion exchange. The similarity in peak positions of XRD data between NLNMO and LLNMO illustrates the phase transition from the original P2 to an O2 phase, further reflecting the Li<sup>+</sup> intercalation during discharging (Table S5).[10a] Nonetheless, it is worth mentioning that a small peak appeared around 16°, which is associated with the persistence of a minor amount of P2 phase due to an incomplete phase transition. This impurity might be harmful for the stability of homogeneous layered structure upon long-term cycling. [10b, 17] However, the O2-type layered structure of LLNMO was obviously maintained during the Li<sup>+</sup> (de)intercalation processes, as demonstrated by the high intensity of the main (002) peak and the absence of any impurity phases. This observation suggests that the structure stability of the O2-type cathode made by chemical ion exchange was superior to the counterpart generated electrochemically (Figure 2b and Table S6).

To further clarify the underlying reasons of irreversible capacity and voltage decay, in-situ DEMS and ex-situ Raman spectroscopy were employed for NLNMO and LLNMO. At the end of initial charging, serious O2 release can be clearly detected within NLNMO, delivering 376.6 µmol O<sub>2</sub> loss per mol of active material (Figure 2c). The evolution gaseous O<sub>2</sub> can only be attributed to arise from oxidized lattice oxygen species. Since the O<sub>2</sub> evolution from the lattice oxygen is a 4e<sup>-</sup> process, the irreversible capacity from the oxygen loss can be calculated to be 40.3 mAh g<sup>-1</sup> within NLNMO.<sup>[3a]</sup> As a sharp comparison, a limited capacity loss (8.4 mAhg<sup>-1</sup>, 78.7 umol O2 loss per mol of electrode) can be achieved with LLNMO during initial charging. Furthermore, the destructive O2 release was effectively restrained in LLNMO during the second charge, compared to a persistently high generation of this gas in NLNMO at the same stage. Ex-situ Raman spectra were employed to probe the local structure change within these two cathodes, which cannot be detected by XRD analysis (Figure 2d). For NLNMO, compared with pristine state, the spectrum of 2<sup>nd</sup> discharged sample showed the same position of main peak at 595 cm<sup>-1</sup> (attributed to the symmetric A<sub>1g</sub> mode) while a wide shoulder occurs at ~630 cm<sup>-1</sup>.<sup>[18]</sup> In turn, the Raman spectrum from a sample after the 5<sup>th</sup> discharge exhibits striking changes, delivering a blue shift (from 595 to 645 cm<sup>-1</sup>) and pronounced broadening of the main peak (~645 cm<sup>-1</sup>), which are indeed associated with the formation of a cubic spinel phase (~630 cm<sup>-1</sup>).<sup>[19]</sup> Moreover, the increase of full width-at-half maximum (FWHM) of the A<sub>1g</sub> Raman mode (TM-O stretching) might be associated with the formation of cationic disorder and oxygen stacking faults upon cycling.<sup>[20]</sup> Furthermore, the disappearance of a group of peaks centered at ~480 cm<sup>-1</sup> can be ascribed to irreversible TM migration into the alkali metal layer. This TM migration leads to the creation of a spinel-like cation arrangement, which is consistent with the previous literature reports of Li<sub>2</sub>MnO<sub>3</sub>.<sup>[21]</sup> These changes in Raman spectra indicate that the layered structure of pristine NLNMO converts to cubic spinel-like structure during cycling, which is in good agreement with the voltage decay and capacity loss observed in electrochemical studies. In contrast, the Raman spectra of LLNMO both after the 2<sup>nd</sup> and 5<sup>th</sup> discharges show similar features, particularly, position and FWHM of the A<sub>1g</sub> mode, to the pristine state. This spectral stability demonstrates that the hexagonal layered structure of LLNMO was maintained, without layered-to-spinel transition, during cycling, which provides a solid foundation for electrochemical stability in long-term cycling.

### 2.2 Cationic/Anionic Valence State Analyses

To further investigate the charge compensation mechanism in Li-excess O2-type LLNMO, Ni and Mn K-edge hard X-ray absorption spectroscopy (XAS) were employed during the two initial Li<sup>+</sup> (de)intercalation cycles. The oxidation state of both Ni and Mn during charging and discharging can be deduced from the variation in the threshold of the absorption edge (Figure 3), aided by the 1st derivative curves. A semiquantitative estimation of the oxidation state of Ni/Mn at different states was performed by applying an integral method in the literature.<sup>[23]</sup> In the first place, the method was employed to give linear relationship between Mn/Ni oxidation states of standard references and edge positions regardless of the edge shape (Figure 3c and

3d). Moreover, approximate average Mn/Ni oxidation states of LLNMO at different charged sates can be deduced in the linear dashed line of reference samples. The detailed data processing is also shown in Figure S6 and S7. The contribution of Ni/Mn-based and oxygen to the redox reactions at different states could thus be concluded (Figure S8).

Compared with the standard spectrum collected from Ni<sup>2+</sup> (Figure S4), the pristine state of Ni within LLNMO was found to be consistent with +2. After charging to 4.8 V, the Ni K-edge shifted toward higher photon energy (green trace), indicating an increase in oxidation state from Ni<sup>2+</sup> to an average value above Ni<sup>3+</sup>, but not quite reaching Ni<sup>4+</sup>, during the initial charge process (Figure 3a). The spectra almost completely shifted back to its original position after discharge to 3.0 V (blue trace), reflecting a nearly reversible reduction process of Ni. After discharge from 3.0 V to 2.0 V, however, there was no significant change of the position of the absorption edge, suggesting Ni redox is not significantly involved at this stage (orange trace). Subsequent recharge to 4.8V induced a shift to a position similar to the first charged state (purple trace). Thus, Ni redox within LLNMO undergoes a relatively reversible process during initial two Li<sup>+</sup> (de)intercalation cycles. In the case of Mn, compared with the reference spectra of MnO<sub>2</sub>, the edge position in the Mn K-edge spectrum of pristine LLNMO was consistent with an initial oxidation state of +4 (Figure S5). During initial charging, the Mn K-edge position stayed constant (green trace), revealing that the Mn oxidation state remained +4 (Figure 3b) and did not participate in the oxidation. However, the Ni oxidation reactions alone cannot compensate all the

charges equivalent to the observed charge capacity, suggesting the existence of the possible oxygen-related redox in this stage, similar to conventional Li-rich layered oxides. [7a, 22] Upon discharge to 3.0 V, the valence state of Mn remained unchanged, indicating Mn redox was also not involved at this high voltage range (blue trace). However, an obvious low-energy shift of the absorption edge can be observed after discharge to 2.0 V, with the absorption edge approaching Mn<sup>3+</sup> (orange trace). This observation indicates a reduction of Mn, whereas Ni did not participate in this low-voltage range. The partial manganese reduction occurs at potentials below 3 V during discharging is in agreement with previous studies of other lithium-rich layered 3d-metal oxides. [22] All in all, Mn remained inactive during charge/discharge processes between 3.0 and 4.8 V but involved in the process between 2.0 and 3.0 V during initial cycle. After recharge to 4.8 V, the spectrum approached the pristine state (purple trace), indicating Mn ions are re-oxidized to Mn<sup>4+</sup>, thus showing a reversible cationic redox process during the second cycle.

# 2.3 Analysis of the Behavior of Oxygen

Further in-depth probing of oxygen-related activity within LLNMO were carried out by *ex-situ* X-ray photoelectron spectroscopy (XPS) and *operando* Raman spectroscopy (Figure 4). For pristine LLNMO, the O 1s XPS peak corresponding to lattice oxygen (O<sup>2-</sup>) is located at 529.3 eV. Besides, peaks at higher binding energy are assigned to oxygenated species deposited on the surface including C=O (531.1 eV) and C-O (532.8 eV) environments (Figure 4a). [24] After charging to 4.8 V, a new shoulder appears at around 530.8 eV, which has been ascribed to the formation of

electron-depleted oxo species (O<sup>n-</sup>). This peak is visually less evident after discharge to 3.0 V and disappears after discharge to 2.0 V, indicating reversibility of the lattice oxygen during initial discharging. Notably, the peak of peroxo-related species can be obtained again when the LLNMO are recharged to 4.8 V, which is consist with previous results observed in lithium-rich layered oxides,<sup>[25]</sup> suggesting a sustained reversible oxygen redox process within LLNMO. A fit of the spectra after the 1<sup>st</sup> charge shows that the relative amount of O2<sup>n-</sup> is ~11.4% with respect to the initial lattice oxygen component, which is in accordance with the capacity distribution (~67 mAh/g based on O2<sup>-</sup>/O2<sup>-</sup>) of oxygen redox during initial charge process. Furthermore, etching was conducted on the electrode in order to confirm the persistence of the signal up to ~100 nm into its bulk. With increasing of the probing depth, there was minimal decrease in the value of relative amount of O<sup>n-</sup> (Figure 4b), further indicating that oxygen redox was not constrained to the surface.

The stretching of the O–O bond (795  $\sim$  845 cm<sup>-1</sup>) detected via *in-situ* Raman spectroscopy of LLNMO confirms the formation of peroxo species during the initial two charges (Figure 4c), unraveling the existence of lattice oxygen redox. These signals vanished upon discharge to 2.0 V, reflecting that the peroxo species can be reversibly reduced back to the initial state (Figure 4c). Similarly, the Raman signals of the peroxo species can also be observed in NLNMO during initial charging, revealing the activation of the oxygen redox chemistry within NLNMO. In addition, a sharp peak appears at  $\sim$ 1104 cm<sup>-1</sup> at the end of the initial charge, revealing the formation of superoxo species ( $O_2^-$ ). The superoxo species is not stable and will be further

oxidized to O<sub>2</sub>, leading to a significant gas evolution, congruous with the observations of DEMS. However, distinctive from NLNMO, this irreversible oxygen behavior (superoxo species) cannot be detected for LLNMO, which could explain the much less O<sub>2</sub> evolution observed in DEMS (Figure 2c). Therefore, *operando* Raman spectroscopy results further illustrate the reversibility of anionic redox reactions within LLNMO, which is consistent with the changes obtained by XPS.

# 2.4 Reversible Structure Evolution and stable electrochemical performance

Next, operando XRD was conducted to evaluate the reversibility of the structural evolution of LLNMO upon the first two Li<sup>+</sup> (de)intercalation cycles (Figure 5a). During initial charging, the (002), (004) and (006) peaks obviously shift to higher angle, indicating the c-lattice parameter rapidly decreases in this process, which can be attributed to the shrinkage of TM layer caused by oxidation reactions of Ni<sup>2+</sup> or/and lattice oxygen. Furthermore, these peaks shift to lower angle than the original state after the first discharge, indicating more Li ions are inserted to alkali metal layer beyond its initial composition, which is consistent with a higher capacity during discharge than charge (Figure 1d). Moreover, the evolution of peak positions upon the second charge exhibits a reverse trend relative to the initial discharge. After the first two cycles, there is no phase transition within LLNMO electrode, demonstrating a good preservation of the trigonal O2-type structure during Li<sup>+</sup> (de)intercalation processes. Even after 50 cycles, the layered structure and O2-type oxygen stacking can be maintained (Figure 5b and Table S7), revealing that LLNMO has excellent structural stability during long-term cycling.

In addition, the normalized discharge curves and corresponding dQ/dV profiles between the 2nd and 50th cycles are shown to investigate the long-term electrochemical performance of LLNMO (Figure 5c). It is worth mentioning that the two pseudo-plateaus located at 3.67 and 2.73 V are well preserved and the positions of corresponding dQ/dV peaks remain constant, indicating the voltage decay can be effectively suppressed during long cycling. At the low current density of 10 mA g<sup>-1</sup> (Figure 5d), limited capacity decay (average capacity drop of 0.15 % upon 100 cycles) and superior coulombic efficiency can be achieved, which indicates stable anionic/cationic redox processes and excellent structure stability can be realized simultaneously within LLNMO during long-term cycling.

#### 3. Conclusion

In this work, O2-type Li<sub>0.66</sub>[Li<sub>0.12</sub>Ni<sub>0.15</sub>Mn<sub>0.73</sub>]O<sub>2</sub> was developed as cathode material via a specific chemical ion-exchange procedure, inheriting the layered structure and Li-excess state within transition metal layer from P2-type Na-based oxide precursor. Reversible oxygen/TM redox reactions can be achieved in LLNMO, which is comprehensively demonstrated by the combination of hard XAS and XPS. Moreover, the layer-to-spinel phase transition and lattice oxygen loss are effectively suppressed within LLNMO, delivering robust structure stability and excellent electrochemical reversibility during long-term cycling. By contrast, a similar O2-type compound harvested by an electrochemical substitution procedure presents severe oxygen loss and voltage decay although it is evolved from the same

sodium-based precursor. Altogether, chemical ion-exchange strategy can be regarded as an efficient way to optimize anionic/cationic redox chemistry within lithium-rich materials, which will offer further unexplored opportunities in securing better structural reversibility and energy retention.

### **Appendix A. Supporting Information**

Experimental section, materials characterization, hard X-ray photoelectron spectroscopy (XAS) measurements, operando shell-isolated nanoparticle-enhanced Raman spectroscopy (SHINERS) measurements, operando Differential Electrochemical Mass Spectrometry (DEMS) measurements and electrochemical measurements.

### **CRediT** authorship contribution statement

Xin Cao: Conceptualization, Methodology, Software, Writing – original draft. Haifeng Li: Visualization, Investigation, Formal analysis. Yu Qiao: Visualization, Investigation, Supervision. Min Jia: Investigation. Ping He: Investigation. Jordi Cabana: Investigation, Formal analysis. Haoshen Zhou: Supervision.

# **Declaration of Competing Interest**

The authors declare that they have no known competing financial interests or personal relationships that could have appeared to influence the work reported in this paper.

# Acknowledgements

X. C. and H. L. contributed equally to this work. This research was partially supported by the National Key Research and Development Program of China (2016YFB0100203) and the National Natural Science Foundation of China (21633003, U1801251). This research used resources of the Advanced Photon Source, a U.S. Department of Energy (DOE) Office of Science User Facility operated for the DOE Office of Science by Argonne National Laboratory under Contract No. DE-AC02-06CH11357. H. L. and J. C. were supported by the National Science Foundation under Grant No. DMR-1809372. X. C. acknowledges the scholarship from the China Scholarship Council (CSC).

#### References

- [1] B. Li, D. Xia, Adv. Mater. 2017, 1701054.
- [2] a) Y. Zuo, B. Li, N. Jiang, W. Chu, H. Zhang, R. Zou, D. Xia, *Adv. Mater.* **2018**, *30*, 1707255; b) N. Yabuuchi, K. Yoshii, S.-T. Myung, I. Nakai, S. Komaba, *J. Am. Chem. Soc.* **2011**, *133*, 4404; c) U. Maitra, R. A. House, J. W. Somerville, N. Tapia-Ruiz, J. G. Lozano, N. Guerrini, R. Hao, K. Luo, L. Jin, M. A. Pérez-Osorio, F. Massel, D. M. Pickup, S. Ramos, X. Lu, D. E. McNally, A. V. Chadwick, F. Giustino, T. Schmitt, L. C. Duda, M. R. Roberts, P. G. Bruce, *Nat. Chem.* **2018**, *10*, 288; d) B. M. d. Boisse, S. I. Nishimura, E. Watanabe, L. Lander, A. Tsuchimoto, J. Kikkawa, E. Kobayashi, D. Asakura, M. Okubo, A. Yamada, *Adv. Energy Mater.* **2018**, *8*, 1800409; e) Y. Qiao, S. Guo, K. Zhu, P. Liu, X. Li, K. Jiang, C.-J. Sun, M. Chen, H. Zhou, *Energy Environ. Sci.* **2018**, *11*, 299.
- [3] a) J. Rana, J. K. Papp, Z. Lebens-Higgins, M. Zuba, L. A. Kaufman, A. Goel, R. Schmuch, M. Winter, M. S. Whittingham, W. Yang, B. D. McCloskey, L. F. J. Piper, *ACS Energy Letters* **2020**, *5*, 634; b) Z. Lun, B. Ouyang, Z. Cai, R. J. Clément, D.-H. Kwon, J. Huang, J. K. Papp, M. Balasubramanian, Y. Tian, B. D. McCloskey, H. Ji, H. Kim, D. A. Kitchaev, G. Ceder, *Chem* **2019**, *6*, 153; c) C. Zhan, Z. Yao, J. Lu, L. Ma, V. A. Maroni, L. Li, E. Lee, E. E. Alp, T. Wu, J. Wen, Y. Ren, C. Johnson, M. M. Thackeray, M. K. Y. Chan, C. Wolverton, K. Amine, *Nat. Energy* **2017**, *2*, 963.
- [4] a) G. Assat, J.-M. Tarascon, *Nat. Energy* **2018**, *3*, 373; b) K. Ku, J. Hong, H. Kim, H. Park, W. M. Seong, S. K. Jung, G. Yoon, K. Y. Park, H. Kim, K. Kang, *Adv. Energy Mater.* **2018**, *8*, 1800606; c) J. Zheng, S. Myeong, W. Cho, P. Yan, J. Xiao, C. Wang, J. Cho, J. G. Zhang, *Adv. Energy Mater.* **2016**, *7*, 1601284.
- [5] a) G. Assat, S. L. Glazier, C. Delacourt, J.-M. Tarascon, *Nat. Energy* 2019, 4, 656;
  b) S. Saha, G. Assat, M. T. Sougrati, D. Foix, H. Li, J. Vergnet, S. Turi, Y. Ha, W. Yang, J. Cabana, G. Rousse, A. M. Abakumov, J.-M. Tarascon, *Nat. Energy* 2019, 4, 977.
- [6] a) T. Teufl, B. Strehle, P. Müller, H. A. Gasteiger, M. A. Mendez, *J. Electrochem. Soc.* **2018**, *165*, A2718; b) N. Li, S. Hwang, M. Sun, Y. Fu, V. S. Battaglia, D. Su, W. Tong, *Adv. Energy Mater.* **2019**, *9*, 1902258.
- [7] a) K. Shimoda, M. Oishi, T. Matsunaga, M. Murakami, K. Yamanaka, H. Arai, Y. Ukyo, Y. Uchimoto, T. Ohta, E. Matsubara, Z. Ogumi, *J. Mater. Chem. A* **2017**, *5*, 6695; b) J. Li, J. Camardese, S. Glazier, J. R. Dahn, *Chem. Mater.* **2014**, *26*, 7059; c) T. Liu, A. Dai, J. Lu, Y. Yuan, Y. Xiao, L. Yu, M. Li, J. Gim, L. Ma, J. Liu, C. Zhan, L. Li, J. Zheng, Y. Ren, T. Wu, R. Shahbazian-Yassar, J. Wen, F. Pan, K. Amine, *Nat. Commun.* **2019**, *10*, 4721.
- [8] M. Gu, I. Belharouak, J. Zheng, H. Wu, J. Xiao, A. Genc, K. Amine, S. Thevuthasan, D. R. Baer, J.-G. Zhang, N. D. Browning, J. Liu, C. Wang, *ACS Nano* **2013**, 7, 760.
- [9] D. Carlier, I. Saadoune, L. Croguennec, M. Menetrier, E. Suard, C. Delmas, *Solid State Ionics* **2001**, *144*, 263; b) A. Clearfield, *Chem. Rev.* **1988**, *88*, 125.
- [10]a) D. L. J. M. Paulsen, J. R. Dahn, *J. Electrochem. Soc.* **2000**, *147*, 2862; b) H. Kim, D.-H. Kwon, J. C. Kim, B. Ouyang, H. Kim, J. Yang, G. Ceder, *Chem. Mater.*

- **2019**, 31, 2431; c) J. M. Paulsen, J.R. Dahn, Solid State Ion. **1999**, 126, 3.
- [11] a) J. M. Paulsen, J. R. Dahn, *J. Electrochem. Soc.* **2000**, *147*, 2478; b) J. Cabana, N. A. Chernova, J. Xiao, M. Roppolo, K. A. Aldi, M. S. Whittingham, C. P. Grey, *Inorg. Chem.* **2013**, *52*, 8540; c) K. Kang, Y. S. Meng, J. Breger, C. P. Grey, G. Ceder, *Science* **2006**, *311*, 977.
- [12] J. M. Paulsen, C. L. Thomas, J. R. Dahn, J. Electrochem. Soc. 1999, 146, 3560.
- [13]a) D. Eum, B. Kim, S. J. Kim, H. Park, J. Wu, S. P. Cho, G. Yoon, M. H. Lee, S. K. Jung, W. Yang, W. M. Seong, K. Ku, O. Tamwattana, S. K. Park, I. Hwang, K. Kang, *Nat. Mater.* **2020**, *19*, 419; b) D. Carlier, A. V. d. Ven, C. Delmas, G. Ceder, *Chem. Mater.* **2003**, *15*, 2651.
- [14] R. Stoyanova, D. Carlier, M. Sendova-Vassileva, M. Yoncheva, E. Zhecheva, D. Nihtianova, C. Delmas, *J. Solid State Chem.* **2010**, *183*, 1372.
- [15] J. M. Paulsen, C. L. Thomas, J. R. Dahn, J. Electrochem. Soc. 2000, 147, 861.
- [16]a) F. Tournadre, L. Croguennec, I. Saadoune, D. Carlier, Y. Shao-Horn, P. Willmann, C. Delmas, *J. Solid State Chem.* **2004**, *177*, 2790; b) F. Tournadre, L. Croguennec, P. Willmann, C. Delmas, *J. Solid State Chem.* **2004**, *177*, 2803.
- [17] H. Gwon, S. W. Kim, Y. U. Park, J. Hong, G. Ceder, S. Jeon, K. Kang, *Inorg. Chem.* **2014**, *53*, 8083.
- [18] S. Francis Amalraj, B. Markovsky, D. Sharon, M. Talianker, E. Zinigrad, R. Persky, O. Haik, J. Grinblat, J. Lampert, M. Schulz-Dobrick, A. Garsuch, L. Burlaka, D. Aurbach, *Electrochim. Acta* **2012**, *78*, 32.
- [19] S. F. Amalraj, L. Burlaka, C. M. Julien, A. Mauger, D. Kovacheva, M. Talianker, B. Markovsky, D. Aurbach, *Electrochim. Acta* **2014**, *123*, 395.
- [20] C. Venkateswara Rao, J. Soler, R. Katiyar, J. Shojan, W. C. West, R. S. Katiyar, *J. Phys. Chem. C* **2014**, *118*, 14133.
- [21] S. F. Amalraj, D. Sharon, M. Talianker, C. M. Julien, L. Burlaka, R. Lavi, E. Zhecheva, B. Markovsky, E. Zinigrad, D. Kovacheva, R. Stoyanova, D. Aurbach, *Electrochimi. Acta* **2013**, *97*, 259.
- [22] M. Oishi, K. Yamanaka, I. Watanabe, K. Shimoda, T. Matsunaga, H. Arai, Y. Ukyo, Y. Uchimoto, Z. Ogumi, T. Ohta, *J. Mater. Chem. A* **2016**, *4*, 9293.
- [23] H. Dau, P. Liebisch, M. Haumann, *Anal Bioanal Chem*, **2003**, *376*, 562.
- [24] X. Bai, M. Sathiya, B. Mendoza-Sánchez, A. Iadecola, J. Vergnet, R. Dedryvère, M. Saubanère, A. M. Abakumov, P. Rozier, J.-M. Tarascon, *Adv. Energy Mater.* **2018**, *8*, 1802379.
- [25] G. Assat, A. Iadecola, D. Foix, R. Dedryvère, J.-M. Tarascon, ACS Energy Letters 2018, 3, 2721.

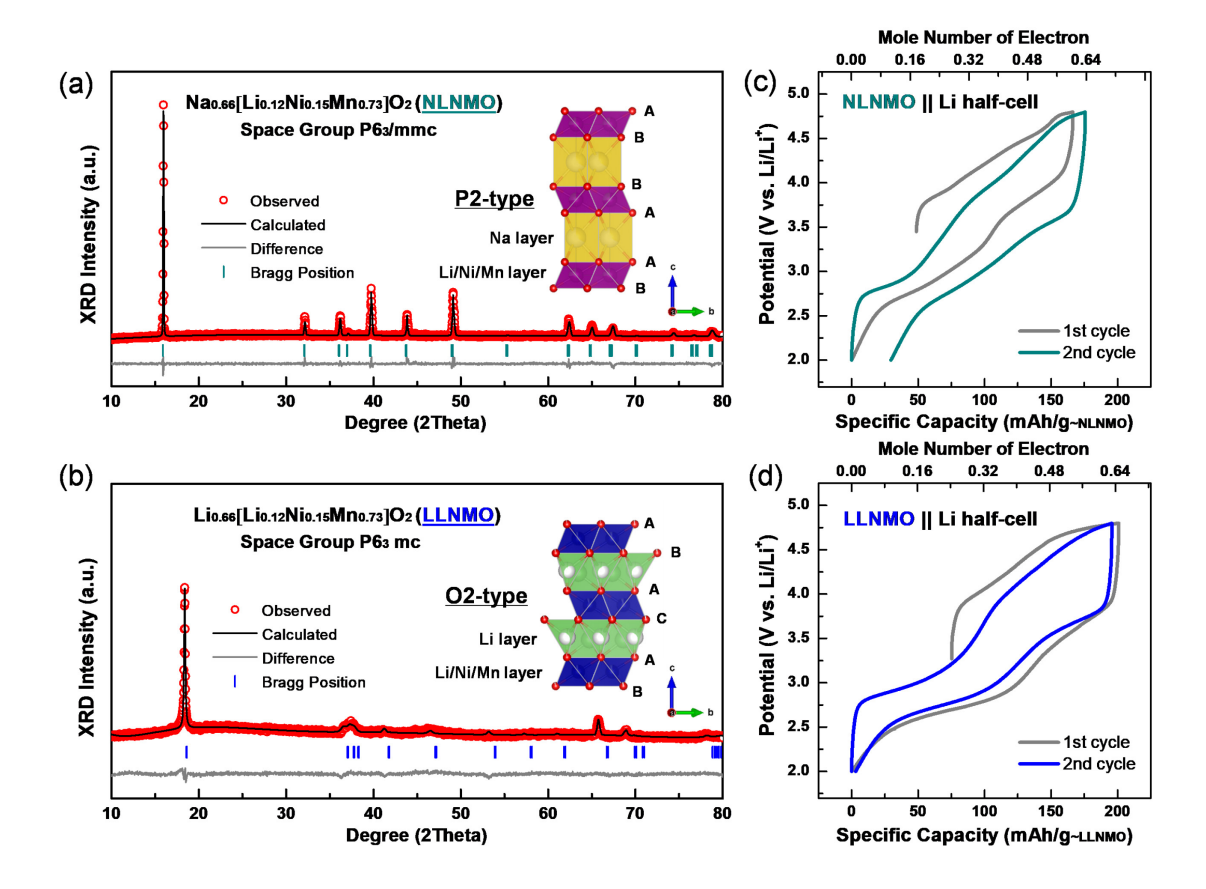
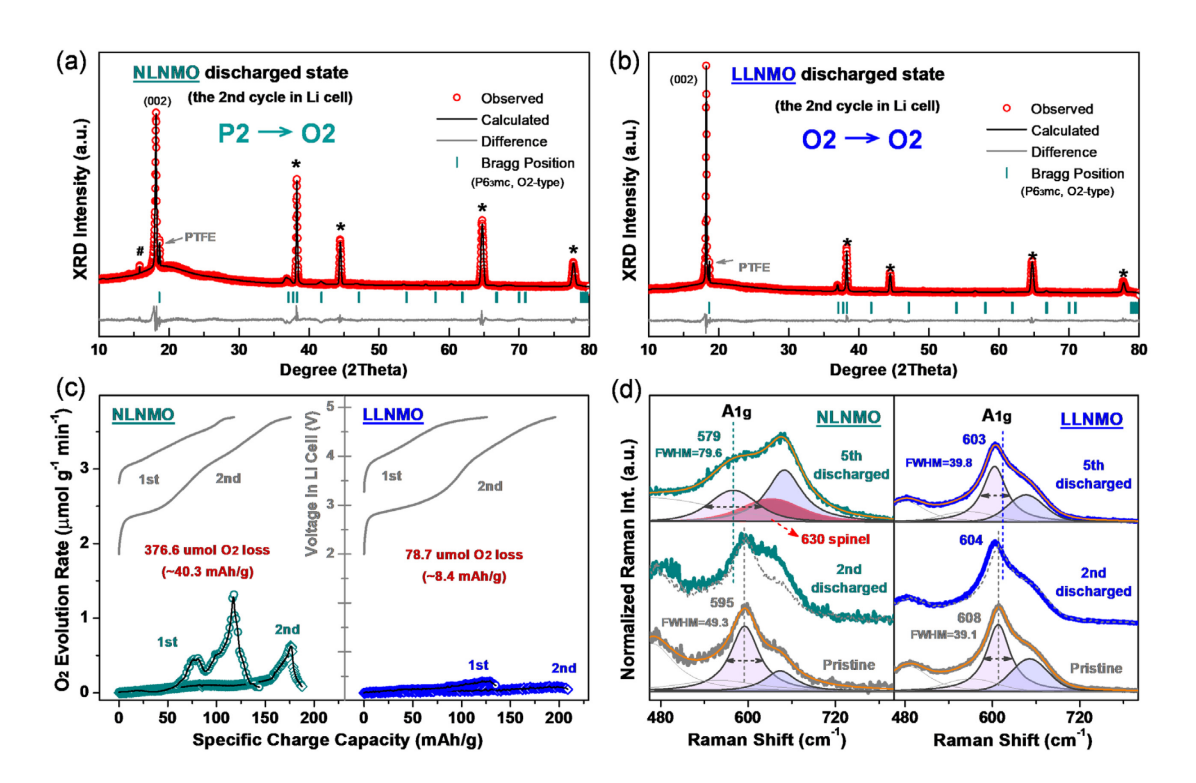
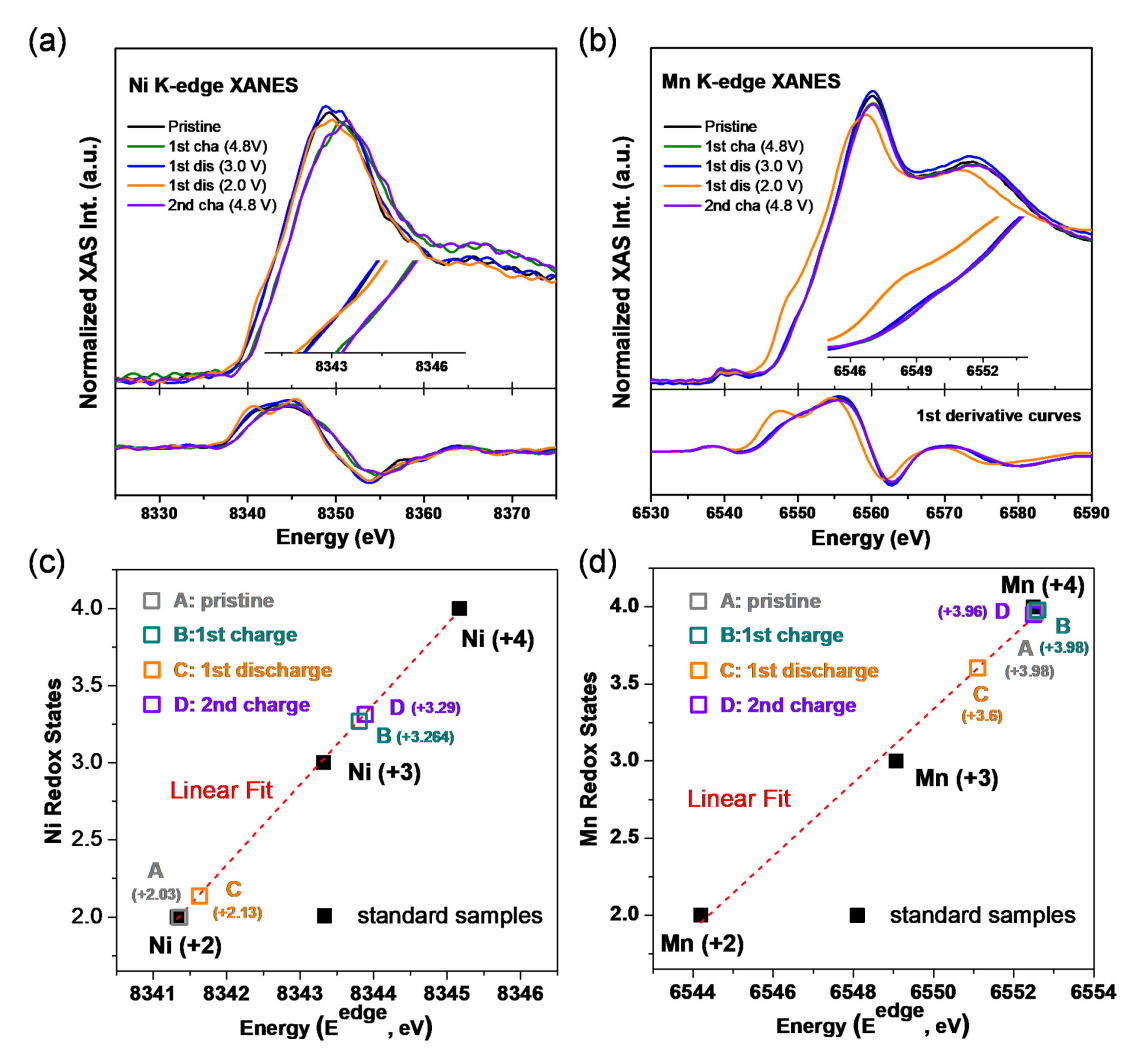


Figure 1. Structural characterization and electrochemical performance of P2-type NLNMO and O2-type LLNMO. The XRD patterns of pristine (a) P2-type NLNMO and (b) O2-type LLNMO. The observed patterns, the calculated patterns, the difference between the two patterns and the corresponding Bragg positions are shown for each XRD pattern. Schematic illustration of the crystal structure of NLNMO with ABBA oxygen stacking and LLNMO with ABAC oxygen stacking are shown as inset for comparison. Typical charge–discharge profiles of (c) NLNMO and (d) LLNMO within the voltage window of 2.0 to 4.8 V at the current density of 10 mA g<sup>-1</sup> in Li-half cells. The number of moles of electron correspond to the moles of (de)intercalated Li<sup>+</sup>/Na<sup>+</sup> during initial two cycles.



**Figure 2.** Structural evolution of NLNMO and LLNMO during cycling. XRD patterns of (a) NLNMO and (b) LLNMO after two cycles, and corresponding results of Rietveld refinement, at the discharged state. The star symbol represents the diffraction peaks from the Al current collector. (c) *Operando* differential electrochemical mass spectrometry (DEMS) of the rate of O<sub>2</sub> evolution from NLNMO and LLNMO during the initial two charges. (d) *Ex-situ* Raman spectra of NLNMO and LLNMO after the 2<sup>nd</sup> and 5<sup>th</sup> cycles, in the discharged state. The Raman spectra of pristine NLNMO and LLNMO are also shown for comparison.



**Figure 3**. Analysis of transition metal activity in LLNMO during the first two cycles. (a) Ni K-edge and (b) Mn K-edge X-ray absorption spectra (XAS) at different states (pristine, 1<sup>st</sup> charged 4.8 V, 1<sup>st</sup> discharged 3.0 V, 1<sup>st</sup> discharged 2.0 V and 2<sup>nd</sup> charged 4.8 V). The corresponding 1st derivative and expanded edge region are also plotted as inset. Evolution of the estimated oxidation state of (c) Mn and (d) Ni during initial two cycles. The linear calibration between Mn/Ni redox states and the K-edge positions is determined by the integral method.

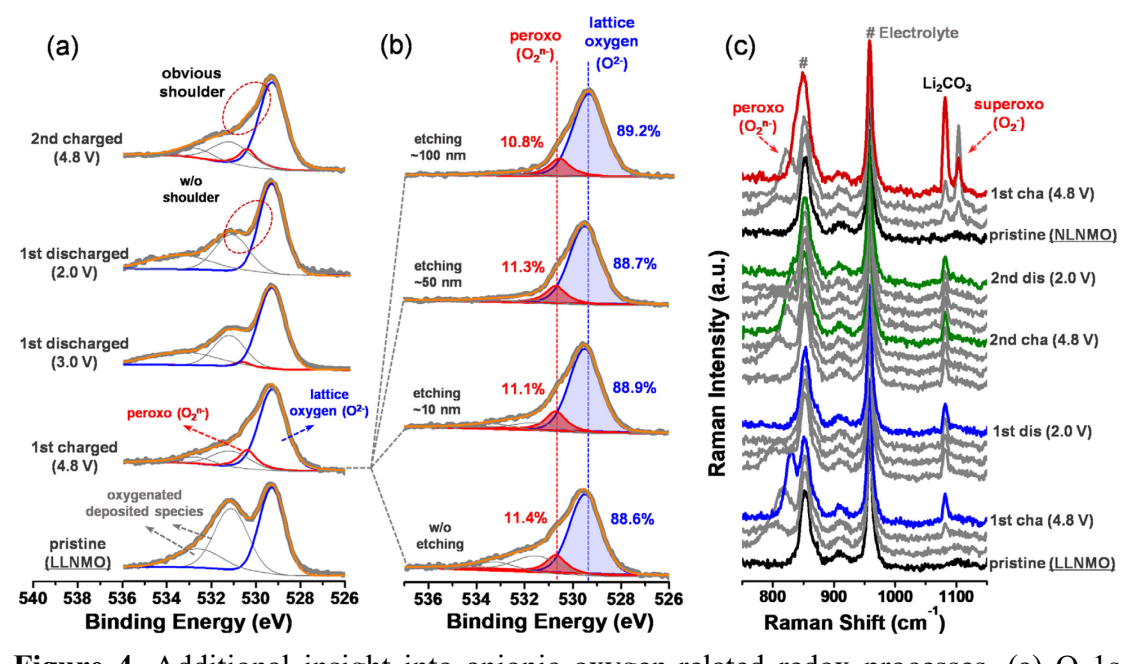


**Figure 4**. Additional insight into anionic oxygen-related redox processes. (a) O 1s XPS spectra of LLNMO collected at different charged states. (Pristine state, 1<sup>st</sup> charged 4.8 V, 1<sup>st</sup> discharged 3.0 V, 1<sup>st</sup> discharged 2.0 V and 2<sup>nd</sup> charged 4.8 V). (b) O 1s XPS spectra of LLNMO collected after the 1<sup>st</sup> charged with different etching depths. (c) Operando Raman spectra of LLNMO and NLNMO collected at different charged states.

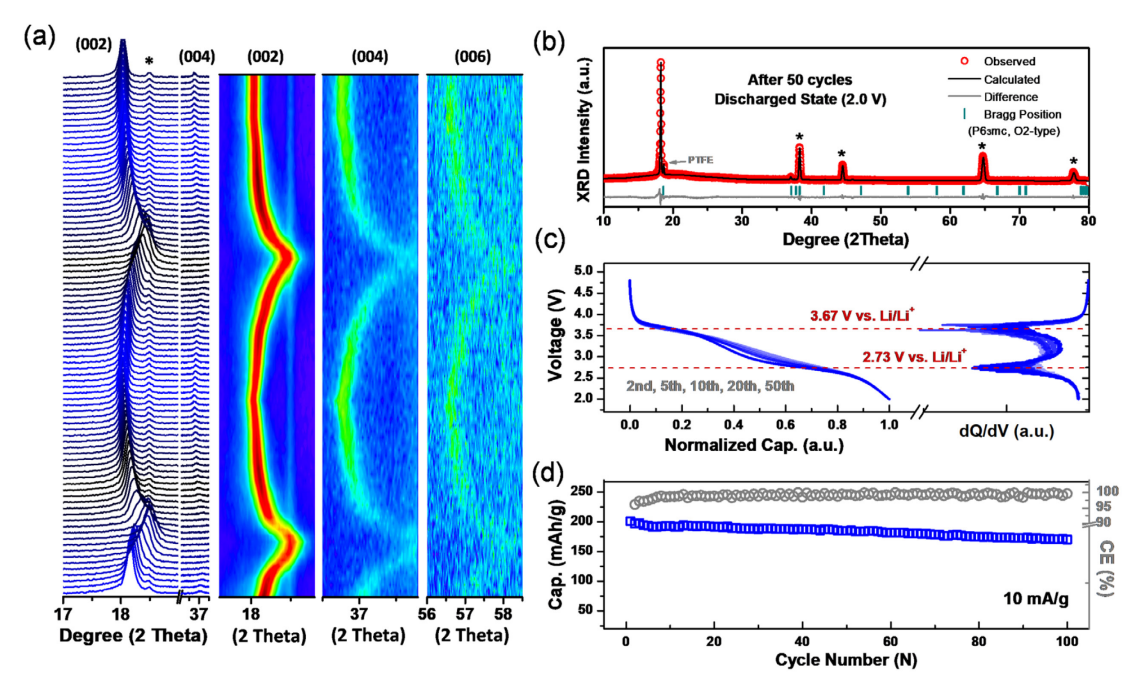


**Figure 5**. Structural evolution processes and electrochemical stability of LLNMO during long-term cycling. (a) Operando XRD patterns of LLNMO electrode during the initial two cycles. The peak around at 18.5° (star symbol) is attributed to binder (PTFE) within electrode. (b) The XRD patterns of LLNMO electrode after 50<sup>th</sup> cycles collected at discharged state. The star symbol represents the diffraction peaks from Al current collector. (c) The normalized discharge profiles of LLNMO and corresponding dQ/dV curves of 2<sup>nd</sup>, 5<sup>th</sup>, 10<sup>th</sup>, 20<sup>th</sup> and 50<sup>th</sup> cycles. (d) The cycling performance of LLNMO between 2 and 4.8 V at the current density of 10 mA g<sup>-1</sup>.